Journal of Physics and Chemistry of Solids 212 (2026) 113565

Contents lists available at ScienceDirect

Journal of Physics and Chemistry of Solids

journal homepage: www.elsevier.com/locate/jpcs

Solution-processed $CdS_{1-x}Se_x$ nanorods with composition-tuned bandgap and microstructural evolution for visible-light photocatalytic response

Suvendu Ghosh [a], Soumya Nandi [b], Soumik De [c], Tanusri Pal [b,*], Surajit Ghosh [a,**]

[a] Optoelectronic Materials Lab, Department of Physics, Vidyasagar University, Midnapore, 721102, India
[b] Department of Physics, Midnapore College, Midnapore, 721101, India
[c] School of Chemical Sciences, National Institute of Science Education and Research (NISER), Jatni, Bhubaneswar, 752050, India

ARTICLE INFO

Keywords:
CdSSe alloy nanorods
Bandgap tuning
Structural anisotropy
Composition-controlled properties
Visible light photocatalysis

ABSTRACT

Compositionally tunable II–VI semiconductor alloys offer a powerful platform for correlating structural evolution with electronic functionality, however such relationships remain insufficiently explored in solution processed systems. Here we report a comprehensive composition resolved investigation of wurtzite $CdS_{1-x}Se_x$ nanorods ($0 \leq x \leq 1$) synthesized via a facile one pot solvothermal route, establishing direct links between alloy stoichiometry, microstructural anisotropy, bandgap modulation, and visible light photocatalytic performance. X-ray diffraction confirms the formation of homogeneous substitutional solid solutions obeying Vegard type lattice expansion, while detailed microstructural analysis reveals pronounced anisotropic crystal growth, with the [002] direction consistently exhibiting larger crystallite size, reduced dislocation density, and lower microstrain compared to the [100] direction, an effect that is maximized at intermediate compositions. Optical absorption and photoluminescence measurements demonstrate continuous bandgap tunability across the visible spectrum, driven by controlled anion substitution and nanoscale confinement. The functional implications of this structural and electronic interplay are highlighted through visible light driven photocatalytic degradation of norfloxacin, where $CdS_{0.8}Se_{0.2}$ exhibits optimal activity, achieving the highest degradation rate constant and lowest electrical energy per order. This superior performance arises from an optimization balance between enhanced visible light absorption, favorable band edge alignment, and defect assisted charge carrier separation. These results elucidate the fundamental origins of anisotropic crystal growth and alloy driven lattice modulation in CdSSe nanorods, and demonstrate compositional engineering as a robust route for tailoring light driven functional performance in solution processable semiconductor nanomaterials.

1. Introduction

Bandgap engineering in semiconductor alloys is a powerful strategy for tailoring electronic structure, enabling precise modulation of optical absorption, excitonic behavior, and charge-carrier dynamics [1–4]. In compositionally tunable II-VI chalcogenides, the electronic bandgap depends strongly on alloy stoichiometry, allowing optical transitions to be positioned across broad spectral ranges without altering the primary crystal framework [5–8]. Such tunability forms the scientific basis for advancing multiple optoelectronic technologies including photodetectors, photovoltaics and light-emitting devices [9–11], where systematic correlations between composition, structure, and electronic response are essential for the designing of a functional material. Despite extensive efforts on quantum dots, thin films, and vapor-phase heterostructures, a comprehensive understanding of how controlled anion substitution influences lattice distortion, crystallographic anisotropy, microstrain, and growth direction in solution-processed II-VI alloys remains incomplete.

The $CdS_{1-x}Se_x$ system is particularly attractive because it offers a continuously adjustable bandgap spanning approximately 2.42 eV for CdS [12] to 1.74 eV for CdSe [13], achieved through substitution of sulfur with selenium within the same lattice. Although earlier studies have addressed optical tuning, most have focused on vapor-grown nanowires or thin films, where elevated growth temperatures often obscure the intrinsic microstructural features arising from alloying [14–18]. For solution-processed CdSSe nanostructures, the structural evolution accompanying compositional variation especially changes in

* Corresponding author.
** Corresponding author.
E-mail addresses: tanusripal@midnaporecollege.ac.in (T. Pal), surajit@mail.vidyasagar.ac.in (S. Ghosh).

https://doi.org/10.1016/j.jpcs.2026.113565
Received 30 December 2025; Received in revised form 25 January 2026; Accepted 27 January 2026

lattice parameters, defect generation, crystallite anisotropy, and directional growth preference has not been systematically mapped across the full alloy range. These factors are critically important because they directly influence carrier mobility, exciton recombination, phonon scattering, and the strength of light–matter interactions.

Beyond their optoelectronic relevance, bandgap-tunable II-VI alloys have also attracted interest in visible-light photocatalysis, where controlled electronic structure is essential for optimizing light absorption and adjusting redox potentials [19–23]. In the CdSSe system, selective anion incorporation enables modulation of both the absorption edge and the separation efficiency of charge carriers, parameters that directly influence catalytic performance under broadband or solar illumination. Understanding how alloy composition affects structural disorder, crystallographic anisotropy, and defect-assisted carrier dynamics is therefore important not only for electronic and optical applications but also for evaluating their performance in light-driven chemical processes.

In recent years, chalcogenide-based semiconductor materials, including sulfides and selenides, have attracted significant attention as visible-light-active photocatalysts owing to their tunable band structures, suitable redox potentials, and strong light absorption characteristics. Recent studies have demonstrated that rational strategies such as compositional modulation, heterojunction construction, cocatalyst integration, and interfacial charge redistribution can effectively enhance charge separation and photocatalytic efficiency in these systems. Notably, a series of recent reports have highlighted the importance of band alignment engineering and S-scheme or Z-scheme charge-transfer pathways in multicomponent chalcogenide photocatalysts, leading to markedly improved photocatalytic performance under visible-light irradiation [24–33].

The present work addresses these knowledge gaps by providing a detailed, composition-resolved study of wurtzite $CdS_{1-x}Se_x$ nanorods synthesized through a one-pot solution route. By examining six distinct alloy compositions from $x = 0$ to $x = 1$, we establish a complete structural and microstructural landscape, demonstrating Vegard-law type linear lattice expansion, composition-dependent peak shifts, and the formation of homogeneous substitutional solid solutions. A consistent and notable observation across intermediate compositions is the superiority of the [002] growth direction, which exhibits larger crystallite size, lower dislocation density, and reduced microstrain compared to the [100] direction. This directional preference, seldom quantified for CdSSe alloys, provides direct insight into anisotropic crystal-growth behavior in solution-processed II-VI chalcogenides.

Complemented by optical absorption and photoluminescence analyses, these results establish a robust structure–composition–property relationship in CdSSe nanorods. Furthermore, by correlating bandgap tuning with visible-light response, we show how moderate lattice perturbation and controlled alloying can influence photocatalytic behavior, expanding the functional scope of these materials. This integrated understanding advances both fundamental alloy science and the potential application of CdSSe nanorods in optoelectronic and light-activated processes.

2. Experimental section

2.1. Chemicals

All reagents used in this study were of analytical grade and were employed directly without any additional purification. Cadmium nitrate tetrahydrate [$Cd(NO_3)_2{\cdot}4H_2O$], sodium selenite (Na_2SeO_3), thiourea (NH_2CSNH_2), and the antibiotic norfloxacin were procured from Sigma-Aldrich, while ethylenediamine (ED), ethylenediaminetetraacetic acid disodium salt (EDTA-Na_2), 2-propanol (IPA) was obtained from Merck.

2.2. Material preparation

The $CdS_{1-x}Se_x$ ($x = 0$, 0.2, 0.4, 0.6, 0.8, 1) ternary alloy nanostructures were prepared through a facile, single-step solvothermal route. In this synthesis the cadmium precursor was kept at a constant molar concentration for all syntheses but the chalcogen precursors were varied to achieve the nominal compositions of $CdS_{1-x}Se_x$ where $x = 0$, 0.2, 0.4, 0.6, 0.8, and 1. In a typical synthesis, stoichiometric amounts of $Cd(NO_3)_2{\cdot}4H_2O$, and NH_2CSNH_2, were dissolved in a mixed solvent system of EN and double-distilled water (DDW) in a 2:1 vol ratio under constant stirring to form a clear homogeneous solution. The resulting mixture was transferred into a Teflon-lined stainless-steel autoclave and maintained at 170 °C for 12 h. After naturally cooling to ambient temperature, the obtained precipitate was repeatedly washed by centrifugation with DDW and IPA to remove residual ions or byproducts. The final $CdS_{1-x}Se_x$ powder with different colours of nanorods was dried overnight at 60 °C and stored for subsequent characterization.

2.3. Materials characterization

X-ray diffraction (XRD) profiles of the $CdS_{1-x}Se_x$ alloy samples were recorded over a 2θ range of 20°–55° using a Rigaku Miniflex diffractometer equipped with Cu K_α radiation ($\lambda = 0.15418$ nm), operated at 30 kV and 10 mA. The surface morphology and structural features were analyzed using field-emission scanning electron microscopy (FESEM; Zeiss Gemini-II Cryo). Transmission electron microscopy (TEM) along with high-resolution TEM (HRTEM) studies were performed on a JEOL F200 microscope operated at 200 kV to examine the crystallinity and nanoscale morphology of the $CdS_{1-x}Se_x$ materials. UV–Vis absorption spectra were recorded using Agilent Cary UV–vis–NIR spectrophotometer in absorption mode using dispersed powder samples; scattering effects inherent to particulate semiconductors may influence the spectral profile. Room temperature Photoluminescence (PL) emission spectra were obtained using a Hitachi F-7000 fluorescence spectrophotometer.

2.4. Measurement of photocatalytic activity

The visible-light photocatalytic performance was evaluated by monitoring the degradation of norfloxacin in the presence of the prepared photocatalysts. Typically, 16 mg of catalyst was dispersed in 40 mL of an aqueous norfloxacin solution (12.5 mg L^{-1}) to form a uniform suspension. The photocatalytic experiments were carried out in a quartz reactor under illumination from a 1000 W tungsten–halogen lamp at ambient temperature. The tungsten–halogen source was chosen for its excellent spectral distribution in the visible region, operational stability, and affordability, providing reproducible laboratory-scale irradiation conditions without requiring high-cost solar simulators. Before exposure to light, the suspension was magnetically stirred in the dark for 30 min to establish adsorption–desorption equilibrium. During illumination, 4 mL aliquots were withdrawn at 5 min intervals and analyzed using UV–visible spectroscopy to track the variation in norfloxacin concentration. The photocatalytic efficiency was estimated from the ratio C/C_0, where C_0 is the initial pollutant concentration and C is its value after an irradiation time t. To minimize thermal interference, the reactor was enclosed within a water-cooled jacket.

3. Results and discussion

3.1. Materials characterization

A digital photograph of the as-synthesized $CdS_{1-x}Se_x$ alloy series was captured under normal visible daylight and is shown in Fig. 1 as the end products. The image vividly demonstrates the systematic evolution of color, progressing from yellow in the S-rich compositions to orange at intermediate stoichiometries and ultimately to deep red and nearly

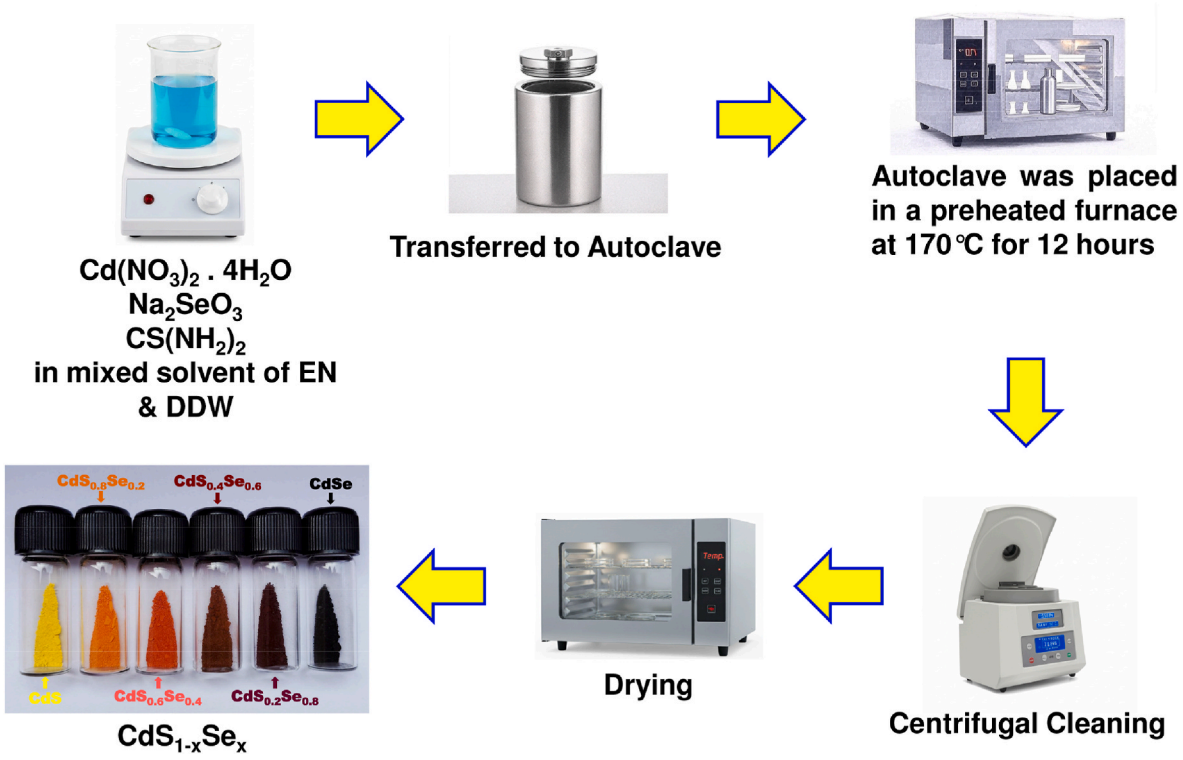

Fig. 1. Schematic illustration of the synthetic pathway used for preparing $CdS_{1-x}Se_x$ alloy nanomaterials, along with real photographs of the obtained $CdS_{1-x}Se_x$ samples with varying sulfur and selenium ratios.

black hues in the Se-rich samples. This progression reflects the compositional dependence of the optical band gap, which decreases from CdS to CdSe. The observed color changes are consistent with the fundamental relationship between band gap energy and perceived color, wherein wider band gaps selectively absorb higher-energy photons, while narrower band gaps extend absorption across the visible spectrum, imparting black. Importantly, digital photography not only provides a compelling qualitative visualization of band gap engineering but, when coupled with digital image colorimetry, can also yield quantitative analysis of colorimetric trends in semiconductor alloys.

The crystallographic features of $CdS_{1-x}Se_x$ nanomaterials were investigated using X-ray diffraction (XRD). As presented in Fig. 2A, the diffraction patterns exhibited broadened reflections with appreciable full width at half maximum (FWHM), which signifies the nanocrystalline nature of the synthesized samples. The characteristic triplet of peaks corresponding to the (100), (002), and (101) planes was observed in all samples. The CdS exhibited sharp diffraction peaks at $2\theta = 24.83°$, 26.49°, 28.20°, 36.63°, 43.73°, 47.83°, 51.86°, 52.85°, and 54.55°, which are indexed to the (100), (002), (101), (102), (110), (103), (112), (201), and (004) planes, respectively, in agreement with the wurtzite phase (JCPDS Card No 41–1049) [34]. In contrast, CdSe displayed reflections at 23.89°, 25.36°, 27.1°, 35.12°, 42.01°, 45.77°, 49.71, 50.71 and 52.07°, which nominally correspond to the same set of planes reported for the wurtzite structure (JCPDS Card No. 08–0459) [35,36]. However, several peak positions appear slightly shifted from the standard wurtzite positions, suggesting either minor contributions from the cubic (zinc blende) phase or strain-induced distortions in the lattice. Overlapping peaks in the 25.36°, 42.01°, and 49.71° regions show potential cubic phase contributions, but these cannot be definitively confirmed without advanced analysis like Rietveld refinement. This ambiguity arises because the only structural difference between hexagonal and cubic CdSe is their close-packing sequence: ABAB for hexagonal and ABCABC for cubic. For the alloyed $CdS_{1-x}Se_x$ samples, the diffraction peaks were found to gradually shift between the positions of CdS and CdSe, confirming the successful formation of a homogeneous solid solution rather than a simple physical mixture of the two binaries. A systematic shift of these peaks to lower Bragg angles with increasing Se content (x) can be attributed to the substitutional incorporation of S^{2-} and Se^{2-} ions within the anion sublattice, as their ionic radii (S^{2-}: 1.84 Å, Se^{2-}: 1.98 Å) and electronegativity values (S: 2.58, Se: 2.55) are

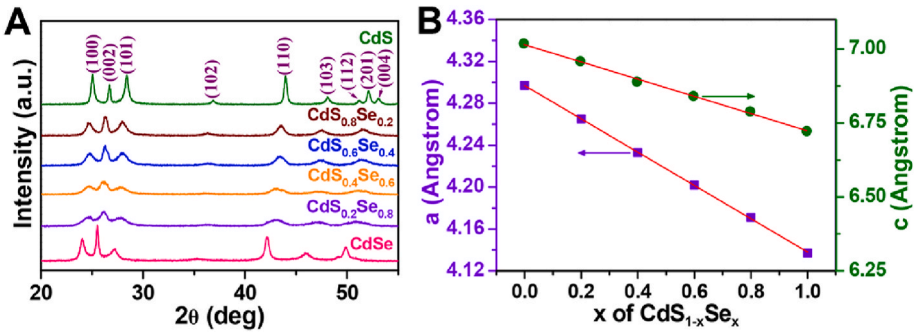

Fig. 2. **(A)** X-ray diffraction (XRD) patterns of $CdS_{1-x}Se_x$ alloys with varying S/Se ratios. **(B)** Compositional variation of lattice parameters *a* and *c* as a function of *x*.

closely matched, facilitating smooth lattice accommodation [37]. Similar shifts have been reported for wurtzite structure in nano-structured $Cd_{1-x}Mn_xSe$ thin films [38]. The characteristic triplet of peaks of the hexagonal morphology corresponding to the (100), (002), and (101) planes was observed in all samples.

The lattice parameters a and c were calculated from the (100) and (002) planes, respectively, using the standard formulae for hexagonal crystals: $\frac{1}{d^2_{(hkl)}} = \frac{4}{3}\frac{h^2+hk+k^2}{a^2} + \frac{l^2}{c^2}$ [39] where $d = \frac{n\lambda}{2\sin\theta}$. Here, d is the interplanar spacing, $(h\,k\,l)$ are the Miller indices, n represents the diffraction order, λ is the X-ray wavelength, and θ is the Bragg angle.

For $(00l)$ reflections, $h = 0$ and $k = 0$, which simplifies the equation: $c = l \times d_{(00l)}$

Considering $(h00)$ peak $(h, k = 0, l = 0)$, gives $a = \sqrt{\frac{4 \cdot d^2_{h00}}{3}}$

In our cases we have used (002) and (100) planes for the calculation of c and a lattice parameter respectively. i.e. $c = l \times d_{(002)}$ and $a = \sqrt{\frac{4 \cdot d^2_{100}}{3}}$

The calculated Lattice Parameters of $CdS_{1-x}Se_x$ alloys are summarized in Table 1 in Supporting Information (SI) and the data is plotted in Fig. 2B. Both lattice parameters a and c follow a linear variation between CdS and CdSe with changing composition (x), closely obeying Vegard's law, thereby confirming the substitutional solid-solution nature of $CdS_{1-x}Se_x$ alloys. The c/a ratio for all composite approaches close to the ideal value for a hexagonal close-packed structure (1.633). The smaller ionic radius of S compared to Se accounts for the contraction in lattice constant with increasing S content, and the measured values are consistent with earlier reports for $CdTe_{1-x}Se_x$ [40], supporting the interpretation that the observed peak splitting arises from subtle lattice distortions that lower the overall symmetry.

The crystallite size of the synthesized particles was determined using the Debye-Scherrer formula [41,42]: $D = K\lambda/\beta \cos\theta$.

In this equation, D represents the average crystallite size, K is the Debye-Scherrer constant (0.94), and β is the full width at half maximum (FWHM) of the diffraction peak. A comparison of D for different composition is presented in Fig. 3A. Furthermore, the dislocation density (δ) [43,44], a parameter that quantifies crystal defects by representing the number of dislocation lines per unit volume of a crystal and the microstrain (ε) [45] were estimated using the following relationship:

$$\delta = \frac{1}{D^2}\ (lines/m^2) \quad and \quad \varepsilon = \frac{\beta\, Cos\,\theta}{4}$$

These values serve as an indicator of the sample's crystallinity. The microstructural parameters like crystallite size, dislocation density and microstrain for the (100) and (002) planes of $CdS_{1-x}Se_x$ series with their terminal alloys CdS and CdSe are presented in Fig. 3B and C, respectively.

The microstructural analysis reveals a pronounced non-monotonic dependence on composition, with crystal quality being optimized at a specific S/Se ratio. The crystallite size reaches a maximum of approximately 50 *nm* at $x = 0.4$, which congruently results in a minimum for both dislocation density ($\sim 0.4 \times 10^{15}\ m^{-2}$) and microstrain (0.31%). This points to the highest crystalline quality with the fewest defects at this composition, an optimum we attribute to a kinetic balance in the incorporation rates of S and Se anions that minimizes lattice strain during growth. In contrast, the terminal compositions $(x = 0, 1)$ and other intermediates exhibit reduced sizes and elevated defect densities. Notably, the $x = 0.8$, composition shows the smallest crystallites and highest dislocation density, likely due to significant lattice distortion from the high Se content.

Furthermore, a consistent anisotropic growth is observed across the series, a characteristic feature of the wurtzite structure. For all intermediate compositions ($x = 0.2$ *to* 0.8), the [002] direction ($c-axis$) is superior to the [100] direction ($a-axis$), exhibiting a larger crystallite size, lower dislocation density, and reduced microstrain, confirming it as the faster and more perfect growth direction. While this anisotropy is minimal in the pure CdS and CdSe end members, the [002] plane still maintains a slight advantage. Overall, the crystal quality is not a linear function of composition but is optimized at $x = 0.4$, with growth consistently favoring perfection along the [002] plane.

The SEM micrographs in Fig. S1 in SI show that all $CdS_{1-x}Se_x$ samples contain uniformly distributed one dimensional nanorods with smooth surfaces and clearly defined boundaries. The images confirm that the synthesis method produces anisotropic chalcogenide nanostructures across the entire alloy series. No secondary particles, spherical impurities, or large agglomerates are visible, which indicates high morphological purity and successful formation of CdSSe solid solutions. Samples containing a smaller amount of selenium exhibit shorter nanorods that appear more closely packed. As the selenium content increases, the nanorods become slightly longer and display better spatial separation. This gradual change in rod dimensions suggests that alloying influences the inherent anisotropic growth behavior while preserving the characteristic one-dimensional morphology. The high degree of uniformity and the clean surface appearance throughout the series show that variation in composition does not disrupt the basic growth process but instead produces controlled and predictable changes in rod elongation.

To gain deeper insight into the internal structure, crystallinity, and nanoscale features of the $CdS_{1-x}Se_x$ alloys with varying Se, TEM was subsequently employed. Fig. 4A presents the low-resolution TEM image of $CdS_{0.8}Se_{0.2}$ nanorods, where the clear nanorod morphology is observed.

Further insight into the crystallinity and atomic structure of the nanorods is provided by the high-resolution TEM (HRTEM) image of $CdS_{0.8}Se_{0.2}$ nanorods shown in Fig. 4B. The image distinctly shows well-resolved lattice fringes, indicating high crystallinity. Two sets of lattice planes can be observed, corresponding to the (100) and (002) planes of the $CdS_{0.8}Se_{0.2}$ hexagonal phase. The measured interplanar spacings are approximately 0.36 nm and 0.34 nm, respectively. The clear visibility of lattice fringes and the absence of significant defects or amorphous regions in the HRTEM image further support the high structural quality of

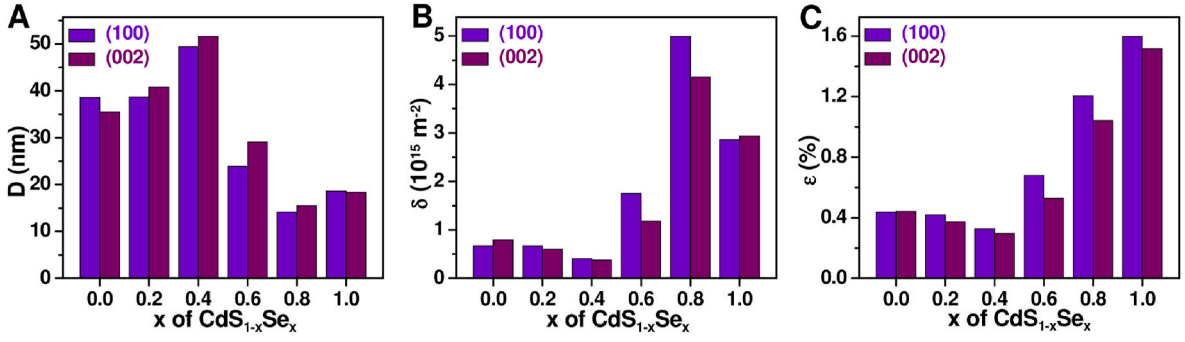

Fig. 3. Variation of **(A)** Crystallite Size, **(B)** Dislocation Density and **(C)** Microstrain of $CdS_{1-x}Se_x$ samples for both (100) and (002) planes with varying S and Se contents.

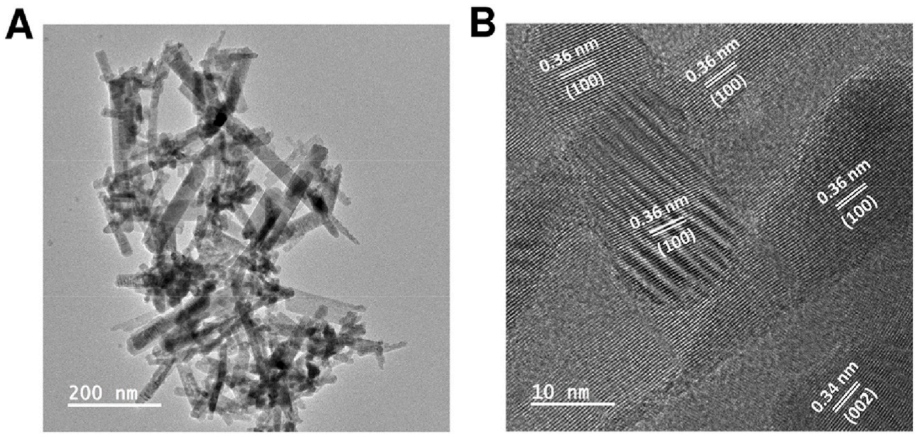

Fig. 4. **(A)** TEM and **(B)** high-resolution TEM (HRTEM) micrographs of the $CdS_{0.8}Se_{0.2}$ alloy.

the synthesized material. This high crystallinity is expected to directly influence their electronic band structure and excitonic behavior. In this context, optical absorption studies were subsequently carried out using UV–Vis spectroscopy to elucidate the composition-dependent bandgap characteristics.

The tunability of the band gap in $CdS_{1-x}Se_x$ nanorods was examined through UV–visible absorption measurements, as shown in Fig. 5A for compositions with x = 0 to 1. The absorption edge positions directly reflect the electronic transition between the valence and conduction bands, enabling comparison of band gap evolution across the alloy series. The optical Band gap were determined from the absorption data using the Tauc method [46] [$\alpha h\nu = A(h\nu - E_g)^n$], as shown in Fig. S2, in SI, and the resulting compositional dependence bandgap is presented in Fig. 5B. In contrast to the bulk CdS and CdSe, the nanorods exhibit a clear blue shift that originates from strong quantum confinement at the nanoscale. In addition, substitution of selenium with the more electronegative sulfur atoms further widens the band gap by altering the electronic structure. As a result, the band gap progressively decreases with higher selenium content, demonstrating that the optical properties of $CdS_{1-x}Se_x$ alloys can be precisely engineered through compositional control. This systematic modulation of the absorption edge strongly suggests corresponding changes in the emission characteristics, which are examined in the subsequent discussion.

Fig. 5C presents the photoluminescence (PL) spectral profiles of $CdS_{1-x}Se_x$ alloy series for a direct comparison. As evident from Fig. 5C, the PL response of the alloys exhibits a systematic blue shift in the emission maxima as the sulfur fraction within the $CdS_{1-x}Se_x$ solid solution increases. This spectral shift originates from the progressive modulation of the bandgap energy caused by the incorporation of smaller-sized S anions in place of Se, which effectively reduces the lattice constant and enhances quantum confinement effects. Consequently, the emission energy of the alloys is tuned toward shorter wavelengths, highlighting the strong composition–structure–optical property correlation in these ternary chalcogenide systems.

3.2. Photocatalytic activity study

The photocatalytic efficiency of the $CdS_{1-x}Se_x$ series was assessed through the visible-light-driven degradation of norfloxacin. Prior to irradiation, the catalyst–pollutant mixtures were stirred in darkness for 30 min to allow adsorption–desorption equilibrium. Subsequent light exposure for 40 min initiated the photocatalytic process. The normalized concentration variation, defined as C/C_o, with C_o representing the initial norfloxacin concentration and C the concentration at time t, is illustrated in Fig. S3A, SI. A steady decrease in pollutant concentration was observed, confirming active photocatalytic degradation. The degradation efficiency (DE) was determined using [47,48]: $DE\,(\%) = \left(1 - \frac{C}{C_o}\right) \times 100\,\%$

The comparative DE values across the alloy series are presented in Fig. 6A. CdS nanorods exhibited ~50% degradation after 40 min of illumination. Incorporating selenium slightly enhanced activity, with $CdS_{0.8}Se_{0.2}$ reaching the highest DE of ~52%. A further increase in Se content, however, resulted in declining performance. A similar compositional trend has been reported for hydrogen evolution in CdSSe solid-solution photocatalysts [49]. These observations suggest that modest selenium incorporation benefits photocatalysis, whereas higher levels exert an adverse influence.

To rationalize the photocatalytic process, kinetic studies were performed within the framework of the Langmuir–Hinshelwood (L–H) model [50,51], which describes surface-mediated reactions influenced

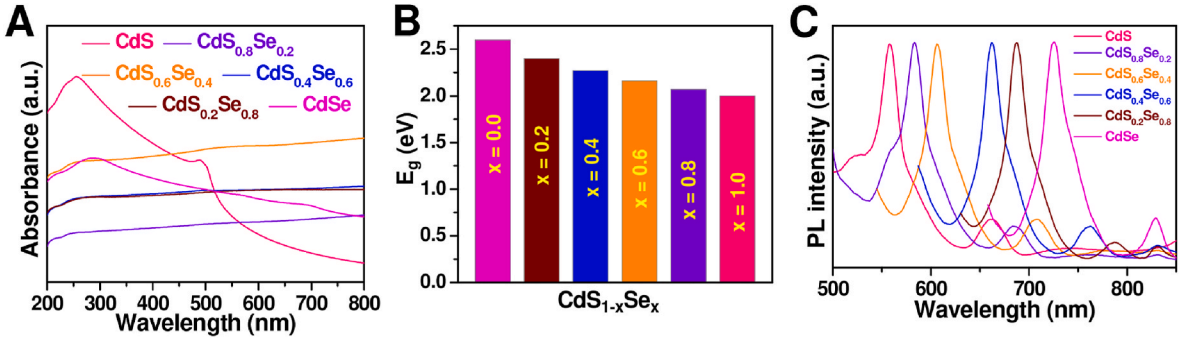

Fig. 5. Optical characterization of $CdS_{1-x}Se_x$ alloys with various S/Se compositions: **(A)** UV–Vis absorption spectra of $CdS_{1-x}Se_x$ samples measured in absorption mode (powder dispersions), **(B)** derived optical bandgap comparison, and **(C)** photoluminescence emission spectra.

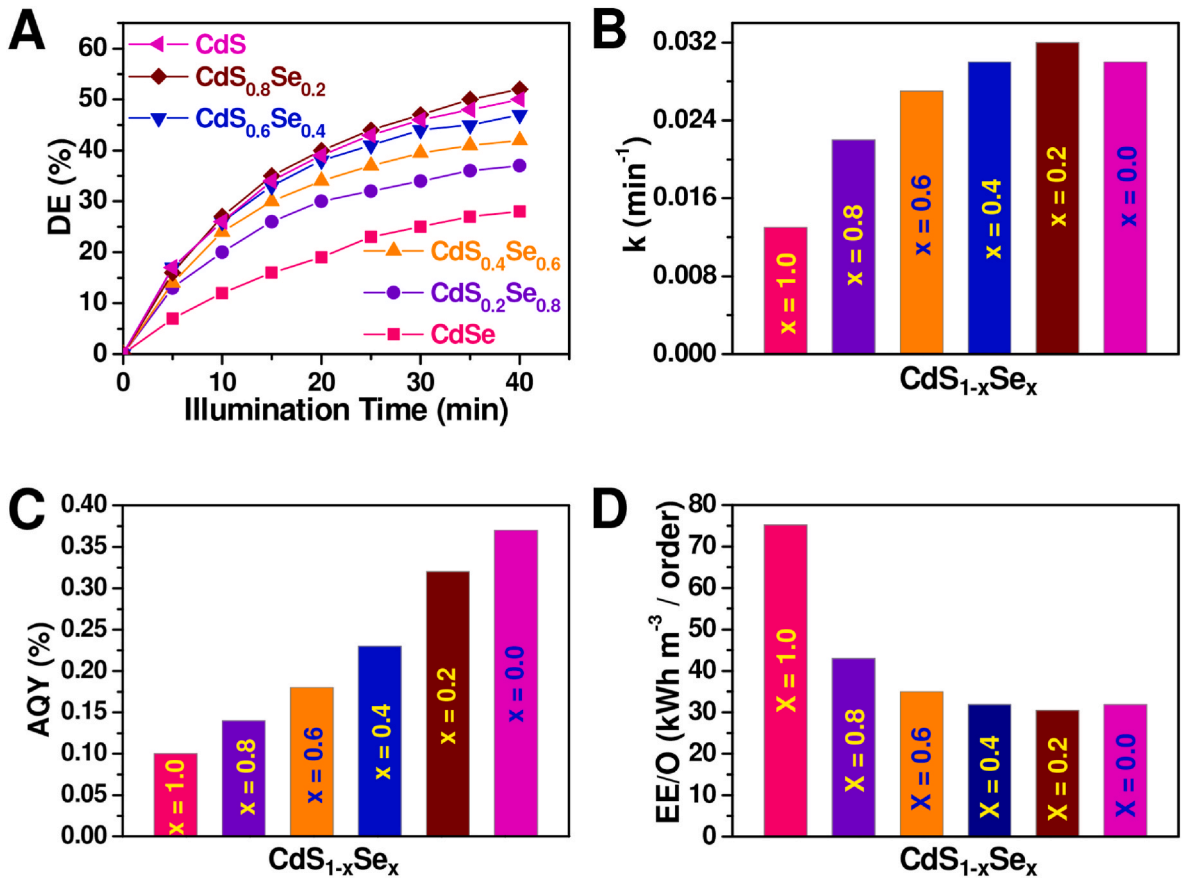

Fig. 6. Evaluation of visible-light-driven photocatalytic behaviour: **(A)** degradation performance, **(B)** reaction kinetics, **(C)** apparent quantum yield (AQY), and **(D)** electrical energy per order (EE/O) values of $CdS_{1-x}Se_x$ with varying x.

by adsorption equilibria. The reaction rate (r, $mg\,L^{-1}\,min^{-1}$) can be written as:

$$r = -\frac{dC}{dt} = \frac{k_r KC}{1+KC}$$

Here, k_r denotes the intrinsic rate constant ($(mg\,L^{-1}\,min^{-1})$, K is the adsorption equilibrium constant ($L\,mg^{-1}$), and C is the pollutant concentration. Under dilute conditions ($KC \ll 1$), the denominator approaches unity, and the equation simplifies to:

$$r = -\frac{dC}{dt} \approx k_r KC$$

where $k = k_r K$ represents the apparent pseudo-first-order rate constant. Integration yields: $ln(C_0/C) = kt$ [52]. Plots of $ln(C_0/C)$ versus irradiation time displayed excellent linearity, validating pseudo-first-order behavior. The extracted rate constants are summarized in Fig. 6B. CdS nanorods showed a rate constant of 0.027 min^{-1}, whereas $CdS_{0.8}Se_{0.2}$ achieved the highest value (0.030 min^{-1}). For higher Se contents, the activity declined, consistent with the *DE* trend.

Since photon flux directly governs carrier generation, the apparent quantum yield (*AQY*) was determined as an efficiency metric. The *AQY* is expressed as [53]:

$$AQY = \frac{Molecule\ degraded}{Incident\ photon} \times 100\ \%$$

The number of incident photons was estimated from the total irradiation energy divided by the photon energy corresponding to the alloy band gap. Upon illumination, excitons formed within CdSSe dissociate into electrons and holes, which subsequently participate in redox reactions. Although white light was employed, only photons overlapping with the material's absorption edge contribute to excitation, implying that the reported *AQY* values underestimate the intrinsic efficiency. As shown in Fig. 6C, CdS exhibited the highest AQY, while the incorporation of Se reduced photon utilization. Nevertheless, $CdS_{0.8}Se_{0.2}$ achieved the second-highest AQY among the CdSSe series.

For practical implementation, the energy cost of photocatalysis is crucial. Energy efficiency was assessed using the *electrical energy per order* (*EE/O*), which quantifies the energy (*kWh*) required to achieve a 90% reduction in pollutant concentration in one cubic meter of solution and was calculated from the slope of $log(C_0/C)$ vs. *Illumination dose* (Fig. S3B, in SI), as [54,55]:

$$\frac{EE}{O} = \frac{Illumination\ dose}{log(C_0/C)}$$

where the illumination dose is given by:

$$Illumination\ dose\ (k\,Wh\,m^{-3}) = \frac{P \times t \times 1000}{V}$$

Here, P is lamp power (kW), t irradiation time (h), and V the treated volume (L). The variation of EE/O with alloy composition is presented in Fig. 6D. $CdS_{0.8}Se_{0.2}$ displayed the lowest EE/O, confirming its superior energy efficiency, while alloys with higher Se fractions exhibited progressively larger values.

The outstanding photocatalytic activity of $CdS_{0.8}Se_{0.2}$ arises from its optimally tuned electronic structure. Incorporating ~20% selenium into the CdS lattice slightly narrows the band gap, extending the absorption edge into the visible-light region and thereby enhancing light harvesting efficiency. At the same time, this modest substitution introduces beneficial lattice perturbations that promote efficient separation and migration of photogenerated electron–hole pairs, effectively

suppressing recombination. As a result, more charge carriers are available to drive surface redox reactions, leading to significantly higher photocatalytic performance. In contrast, alloys with greater selenium content exhibit excessive band-gap narrowing and a shift in band-edge positions that weakens the redox potential. Moreover, increased structural disorder at higher Se concentrations introduces recombination centers, which counteract photocatalytic efficiency. Thus, $CdS_{0.8}Se_{0.2}$ represents the optimum balance between light absorption, charge separation, and redox driving force, explaining its superior activity compared to both CdS and higher Se-substituted alloys.

The $CdS_{0.8}Se_{0.2}$ catalyst demonstrates excellent operational durability, retaining close to ninety percent of its photocatalytic performance after five consecutive runs. To examine whether repeated irradiation and reuse induced any structural modifications, X-ray diffraction profiles were collected for the $CdS_{0.8}Se_{0.2}$ sample following the cycling experiments, and is shown in Fig. S4, in SI. The post-reaction diffraction pattern closely matches that of the initial $CdS_{0.8}Se_{0.2}$, showing no meaningful shifts in peak position or intensity. This consistency confirms that the CdSe maintains its crystalline framework and phase stability during repeated photocatalytic operation, highlighting its suitability for long term environmental applications.

While the microstructural analysis identifies $CdS_{0.6}Se_{0.4}$ having the highest crystallinity, the superior photocatalytic performance of $Cd_{0.8}Se_{0.2}$ can be understood by prioritizing electronic structure and charge carrier dynamics over long-range crystalline perfection. The incorporation of 20% selenium creates mild lattice strain and perturbations, as seen in its slightly reduced crystallite size and increased microstrain compared to $x = 0.4$. However, this level of disorder is not detrimental; instead, it is beneficial. These lattice imperfections act as productive sites that facilitate the crucial separation of photogenerated electron-hole pairs, effectively suppressing their recombination.

Furthermore, this composition provides an optimal electronic balance by narrowing the band gap enough to enhance visible light absorption compared to CdS, while still maintaining favorable band edge positions. In contrast, alloys with higher selenium content such as $x = 0.8$ show a shift in band edges that reduces the redox potential.

Therefore, although $CdS_{0.6}Se_{0.4}$ sample is structurally superior but electronically and catalytically "passive". The $CdS_{0.2}Se_{0.8}$ sample is structurally too defective, creating excessive recombination centers that hinder the catalytic performance. The $CdS_{0.8}Se_{0.2}$ sample, however, occupies a functional optimum. It possesses sufficient crystalline order to allow for charge migration, while the intentional, moderate lattice disorder introduced by Se doping optimally promotes charge separation, making it the most functionally effective photocatalyst.

Interestingly, while the AQY was found to be the highest for CdS, the overall degradation efficiency, rate constant, and EE/O values reached their optimum at the $CdS_{0.8}Se_{0.2}$ composition, exhibiting the highest photocatalytic activity and the lowest energy consumption. This apparent discrepancy arises from the fundamental difference between photon-to-reaction conversion efficiency and total light harvesting. CdS, owing to its wider band gap, absorbs a relatively narrow portion of the visible spectrum; however, the absorbed photons are utilized very efficiently in redox reactions, resulting in a superior AQY. In contrast, the incorporation of Se into the CdS lattice narrows the band gap and redshifts the absorption edge, enabling $CdS_{0.8}Se_{0.2}$ to harvest a substantially larger fraction of the visible spectrum. Although the per-photon efficiency of this alloyed composition is slightly lower due to increased nonradiative recombination and defect-mediated losses, the much higher number of absorbed photons leads to a greater total generation of reactive species, thereby enhancing the overall degradation performance. Thus, $CdS_{0.8}Se_{0.2}$ achieves the best balance between light absorption and charge utilization, making it the most effective photocatalyst composition despite not exhibiting the highest AQY.

In summary, although pure CdS exhibits the highest AQY on a per-photon basis (measured here as an incident-photon AQY at the sample's absorption edge), $CdS_{0.8}Se_{0.2}$ delivers the highest overall degradation efficiency and apparent rate constant under white-light illumination and consequently the lowest EE/O. This outcome reflects an optimal trade-off in $CdS_{0.8}Se_{0.2}$ between broadened light harvesting and sufficiently strong redox potential and charge separation.

Norfloxacin degradation in aqueous media is known to proceed predominantly through oxidative pathways, as widely reported in earlier studies [56,57]. To gain mechanistic insight into the photocatalytic process over $CdS_{0.8}Se_{0.2}$, a series of radical scavenging experiments was conducted to identify the dominant reactive species involved. EDTA–Na_2 was introduced as a hole (h^+) scavenger, IPA was used to suppress hydroxyl radicals ($OH^{\cdot}$), and nitrogen purging was employed to inhibit superoxide radical ($O_2^{-\cdot}$) formation by removing dissolved oxygen from the reaction medium [58–60].

The evolution of normalized norfloxacin absorption peaks in the presence of different scavengers was systematically monitored. The comparisons of photocatalytic degradation efficiencies and apparent rate constant under each condition is summarized in SI as Fig. S5A and Fig. S5B, respectively. The addition of EDTA–Na_2 led to a substantial decline in photocatalytic performance, limiting the degradation efficiency to approximately 14%, which underscores the dominant role of photogenerated holes in initiating norfloxacin oxidation. In contrast, the presence of nitrogen atmosphere and IPA resulted in moderate suppression effects, with degradation efficiencies of about 20% and 35%, respectively, indicating that hydroxyl and superoxide radicals also participate in the degradation process, albeit to a lesser extent.

The photocatalytic degradation of norfloxacin under visible-light irradiation over CdSSe is proposed to proceed through a synergistic oxidative pathway involving multiple reactive species. Upon visible-light excitation ($h\nu$), CdSSe generates electron–hole pairs (e^- /h^+). The photogenerated electrons can interact with dissolved molecular oxygen (O_2) to form superoxide radicals ($O_2^{-\cdot}$), which may subsequently undergo proton-coupled reactions to yield hydroperoxyl radicals ($HO_2^{\cdot}$) and hydrogen peroxide (H_2O_2). The latter can further participate in reduction reactions, producing highly reactive hydroxyl radicals ($OH^{\cdot}$), thereby enhancing the oxidative environment. Simultaneously, photogenerated h^+ are capable of oxidizing surface-adsorbed water or hydroxide species to generate additional $OH^{\cdot}$ radicals.

Consistent with the scavenger experiments, photogenerated holes play a dominant role in initiating norfloxacin oxidation, while superoxide and hydroxyl radicals act as auxiliary reactive species contributing to molecular breakdown. These reactive oxygen species collectively attack the norfloxacin molecule, leading to progressive structural decomposition into degraded products under visible-light illumination. A schematic illustration of the pathway for reactive species generation and the associated photocatalytic degradation of norfloxacin is provided in Fig. S6 in SI.

4. Conclusion

In summary, we have demonstrated a solution-based approach for preparing composition controlled $CdS_{1-x}Se_x$ nanorods and established clear links among alloy composition, structural evolution and electronic response. X-ray diffraction confirmed the formation of homogeneous wurtzite solid solutions with continuous lattice expansion that follows Vegard type behavior. Microstructural analysis revealed pronounced anisotropic crystallite development, with the [002] direction showing larger crystallite size, lower dislocation density and reduced microstrain relative to the [100] direction, providing new insight into directional growth in II-VI alloy nanostructures. Optical measurements showed a predictable redshift in bandgap with increasing selenium content, enabling a direct correlation between composition, lattice perturbation and optical transition energy. The optimized composition displayed an improved visible light response, which translated into enhanced photocatalytic degradation of norfloxacin, demonstrating the functional relevance of controlled alloying.

Overall, these results advance the understanding of substitutional alloy formation and anisotropic crystal growth in CdSSe nanorods and highlight the effectiveness of compositional engineering in tuning structural quality, electronic transitions and light driven functionality. The insights gained here provide a useful framework for designing solution processable semiconductor nanomaterials for optoelectronic and environmental applications.

CRediT authorship contribution statement

Suvendu Ghosh: Writing – original draft, Methodology, Formal analysis, Data curation. **Soumya Nandi:** Formal analysis, Data curation. **Soumik De:** Data curation. **Tanusri Pal:** Writing – review & editing, Funding acquisition, Formal analysis, Conceptualization. **Surajit Ghosh:** Writing – review & editing, Supervision, Investigation, Conceptualization.

Declaration of competing interest

The authors declare that they have no known competing financial interests or personal relationships that could have appeared to influence the work reported in this paper.

Acknowledgments

The authors gratefully acknowledge financial support from the Department of Science and Technology and Biotechnology (DSTBT), Government of West Bengal, India, under Grant No. 625(Sanc)/STBT-11012(26)/2/2024-ST SEC. The authors also appreciate the infrastructural assistance provided by the Department of Science and Technology (DST) and the University Grants Commission (UGC), New Delhi, India, through the FIST and SAP programs to the Department of Physics, Vidyasagar University. The authors further acknowledge the University Science Instrumentation Centre (USIC), Vidyasagar University, for facilitating photoluminescence measurements.

Appendix A. Supplementary data

Supplementary data to this article can be found online at https://doi.org/10.1016/j.jpcs.2026.113565.

Data availability

Data will be made available on request.

References

[1] S. Wang, J. Cavin, Z. Hemmat, K. Kumar, A. Ruckel, L. Majidi, H. Gholivand, R. Dawood, J. Cabana, N. Guisinger, R.F. Klie, F. Khalili-Araghi, R. Mishra, A. Salehi-Khojin, Phase-dependent band gap engineering in alloys of metal-semiconductor transition metal dichalcogenides, Adv. Funct. Mater. 30 (2020) 2004912.

[2] A. Chaves, J.G. Azadani, H. Alsalman, D.R. da Costa, R. Frisenda, A.J. Chaves, S. H. Song, Y.D. Kim, D. He, J. Zhou, A. Castellanos-Gomez, F.M. Peeters, Z. Liu, C. L. Hinkle, S.-H. Oh, P.D. Ye, S.J. Koester, Y.H. Lee, P. Avouris, X. Wang, T. Low, Bandgap engineering of two-dimensional semiconductor materials, npj 2D Mater. Appl. 4 (2020) 29.

[3] R. Sa, Q. Zhang, Y. Yang, D. Liu, Bandgap engineering of $Na_{1-x}Ag_xSbS_2$ alloys for photovoltaic applications, Mater. Res. Bull. 152 (2022) 111862.

[4] A.M. Smith, S. Nie, Semiconductor nanocrystals: structure, properties, and band gap engineering, Acc. Chem. Res. 43 (2010) 190–200.

[5] A. Giri, G. Park, U. Jeong, Layer-structured anisotropic metal chalcogenides: recent advances in synthesis, modulation, and applications, Chem. Rev. 123 (2023) 3329–3442.

[6] D. Mastrippolito, M. Cavallo, H.B. Jalali, G.O. Eren, E. Bossavit, H. Zhang, T. Gemo, A. Colle, A. Khalili, C. Gureghian, Y. Prado, M.G. Silly, D. Pierucci, F.D. Stasio, E. Lhuillier, Tuning electronic properties of II–VI and III–V narrow band gap nanocrystals through exposure to alkali, Chem. Mater. 36 (2024) 11669–11675.

[7] H.E. Ruda (Ed.), Widegap II–VI Compounds for Opto-electronic Applications, Springer, New York, 1992, https://doi.org/10.1007/978-1-4615-3486-0.

[8] A. Kar, K.R. Balasubramaniam, D.S. Monder, Phase diagram, electronic structure, and optical properties of $KCuTe_{1-x}Se_x$ photocathodes: a computational study, ACS Appl. Energy Mater. 8 (2025) 8418–8428.

[9] M. Peng, Z. Wen, X. Sun, Recent progress of flexible photodetectors based on low-dimensional II–VI semiconductors and their application in wearable electronics, Adv. Funct. Mater. 33 (2023) 2211548.

[10] A. Bukhtiar, B. Zou, Low-dimensional II–VI semiconductor nanostructures of ternary alloys and transition metal ion doping: synthesis, optical properties and applications, Mater. Adv. 5 (2024) 6739–6795.

[11] Y.-H. Kim, Y.-W. Kim, S. Choi, S. Kim, S. Park, Y. Kim, S. Ryu, C. Lee, B. Kim, J. Yoo, H. Yang, Efficient, operation-stable green ZnSeTe quantum dot-light-emitting diodes: impacts of shell dimension and Al incorporation, Chem. Eng. J. 522 (2025) 167742.

[12] N. Kumari, S. Dahiya, C. Gautam, P. Maity, S. Chatterjee, B.N. Pal, A.K. Ghosh, Structural, optical, and electronic properties of $Ni_xCd_{1-x}S$ quantum dots: implications for photodetection applications, ACS Appl. Nano Mater. 8 (2025) 15441–15451.

[13] A. Sobhani, M. Salavati-Niasari, Transition metal selenides and diselenides: hydrothermal fabrication, investigation of morphology, particle size and their applications in photocatalyst, Adv. Colloid Interface Sci. 287 (2021) 102321.

[14] Z. Xu, Q. Lv, X. Li, Y. Meng, J.C. Ho, P. Guo, Composition-tunable bandgap engineering of horizontally guided CdS_xSe_{1-x} nanowalls for high-performance photodetectors, ACS Appl. Mater. Interfaces 17 (2025) 1962–1970.

[15] X. Shen, Q. Lv, Q. Yang, J. Fan, X. Song, P. Guo, P. Li, J.C. Ho, K.M. Yu, Two-step magnetic-pulling chemical vapor deposition growth of $CdS_{1-x}Se_x$ lateral nanoribbon heterostructures for high-performance photodetectors, Adv. Photonics Res. 4 (2023) 2200166.

[16] Y. Myung, D.M. Jang, T.K. Sung, Y.J. Sohn, G.B. Jung, Y.J. Cho, H.S. Kim, J. Park, Composition-tuned ZnO−CdSSe core−shell nanowire arrays, ACS Nano 4 (2010) 3789–3800.

[17] Q. Zhang, H. Liu, P. Guo, D. Li, P. Fan, W. Zheng, X. Zhu, Y. Jiang, H. Zhou, W. Hu, X. Zhuang, H. Liu, X. Duan, A. Pan, Vapor growth and interfacial carrier dynamics of high-quality CdS-CdSSe-CdS axial nanowire heterostructures, Nano Energy 32 (2017) 28–35.

[18] X. Zhan, Q. Wang, F. Wang, Y. Wang, Z. Wang, J. Cao, M. Safdar, J. He, Composition-tuned $ZnO/Zn_xCd_{1-x}Te$ core/shell nanowires array with broad spectral absorption from UV to NIR for hdrogen generation, ACS Appl. Mater. Interfaces 6 (2014) 2878–2883.

[19] Q. Li, H. Meng, P. Zhou, Y. Zheng, J. Wang, J. Yu, J. Gong, $Zn_{1-x}Cd_xS$ solid solutions with controlled bandgap and enhanced visible-light photocatalytic H_2-Production activity, ACS Catal. 3 (2013) 882–889.

[20] J. Liu, G. Ren, G. Hu, C. Wang, T. Guo, Q. Guo, P.S. Goh, Enhancing the photocatalytic hydrogen evolution of ZnCdS through induced dipole polarization, J. Phys. Chem. Lett. 16 (2025) 7337–7345.

[21] Y. Wang, X. Zhan, F. Wang, Q. Wang, M. Safdar, J. He, Crystalline ZnO/ZnS_xSe_{1-x} core–shell nanowire arrays for efficient visible-light photoelectrocatalysis, J. Mater. Chem. A 2 (2014) 18413–18419.

[22] W. Huang, S. Ge, Y. Lei, Z. Zheng, Composition-dependent perfect band gap tuning of ZnS_{1-x} Se_x solid solutions for efficient photocatalysis, J. Phys. Chem. Solid. 130 (2019) 41–45.

[23] A.T. Nguyen, W.-H. Lin, Y.-H. Lu, Y.-D. Chiou, Y.-J. Hsu, First demonstration of rainbow photocatalysts using ternary $Cd_{1-x}Zn_xSe$ nanorods of varying compositions, Appl. Catal., A 476 (2014) 140–147.

[24] Q. Chen, Y.-H. Chen, J.-R. Zhu, Z.-Y. Li, F.-X. Xiao, Customizing synchronous charge tunneling photosystems toward solar CO_2 conversion, Adv. Funct. Mater. 35 (2025) 2417139.

[25] M. Lin, Y. He, X. Guo, G. Xiao, F.-X. Xiao, Heterointerface engineering of In_2S_3/Ag_2S S-scheme photocatalyst toward solar hydrogen peroxide photosynthesis, ChemSusChem 18 (2025) e202501827.

[26] L. Cai, Y.-S. Cai, W. Zhao, J. Liang, Q. Chen, F.-X. Xiao, Coupling transition metal chalcogenides with metal nanoclusters for steering photoredox catalysis, Inorg. Chem. 64 (2025) 12815–12823.

[27] X. Guo, S. He, M. Lin, Z. Chen, F.-X. Xiao, Customizing transition metal chalcogenide heterostructure photosystems toward multifarious photoredox catalysis, Inorg. Chem. 64 (2025) 19413–19422.

[28] Y.-B. Li, F.-X. Xiao, Atomically precise metal nanocluster-mediated solar hydrogen production, Inorg. Chem. 64 (2025) 3608–3615.

[29] Y.-B. Li, F.-X. Xiao, Surmounting the instability of atomically precise metal nanoclusters towards boosted photoredox organic transformation, Chem. Sci. 16 (2025) 2661–2672.

[30] L. Cai, Q. Chen, R. Xu, T. Li, J. Liang, F.-X. Xiao, Transition metal chalcogenides/nonconjugated polymer artificial photosystems for photoredox catalysis, Inorg. Chem. 63 (2024) 24382–24391.

[31] Y. Wang, W. Li, W. Duan, R. Cui, G. Liao, N. Wang, Hydrophilicity improvement of PVDF-networked CdS/TiO_2 photocatalytic membrane for flat-panel purification of pharmaceutical wastewater accompanied by Cr(VI) reduction, Chem. Eng. J. 519 (2025) 165220.

[32] H. Qin, W. Li, G. Liao, J. Li, W. Duan, T. Ma, C. Wang, Polyvinylidene fluoride-networked $Sb_2S_3/CdS/Ag_2S$ membrane with dual-junction exciton dynamics for indepth purification of textile printing/dyeing wastewater, ChemSusChem 18 (2025) e202500051.

[33] W. Li, W. Duan, G. Liao, F. Gao, Y. Wang, R. Cui, J. Zhao, C. Wang, 0.68% of solar-to-hydrogen efficiency and high photostability of organic-inorganic membrane catalyst, Nat. Commun. 15 (2024) 6763.

[34] T. Gao, T. Wang, Catalyst-assisted vapor-liquid-solid growth of single-crystal CdS nanobelts and their luminescence properties, J. Phys. Chem. B 108 (2004) 20045–20049.
[35] L.F. Xi, Y.M. Lam, Synthesis and characterization of CdSe nanorods using a novel microemulsion method at moderate temperature, J. Colloid Interface Sci. 316 (2007) 771–778.
[36] N. Mukherjee, G.G. Khan, A. Sinha, A. Mondal, Synthesis of band gap engineered $Pb_XCd_{1-X}Se$ thin films: a study on their optical, electrical, structural and localized mechanical properties, Phys. Status Solidi. A 207 (2010) 1880–1886.
[37] S.-H. Bo, Y. Wang, G. Ceder, Structural and Na-ion conduction characteristics of $Na_3PS_xSe_{4-x}$, J. Mater. Chem. A 4 (2016) 9044–9053.
[38] A.H. Eid, M.B. Seddek, A.M. Salem, T.M. Dahy, Structural characterization and optical properties of $Cd_{(1-x)}Mn_xSe$ thin films, Vacuum 83 (2008) 401–407.
[39] R. Sonkar, N.J. Mondal, B. Boro, M.P. Ghosh, D. Chowdhury, Cu doped ZnO nanoparticles: correlations between tuneable optoelectronic, antioxidant and photocatalytic activities, J. Phys. Chem. Solid. 185 (2024) 111715.
[40] M. Lingg, A. Spescha, S.G. Haass, R. Carron, S. Buecheler, A.N. Tiwari, Structural and electronic properties of $CdTe_{1-x}Se_x$ films and their application in solar cells, Sci. Technol. Adv. Mater. 19 (2018) 683–692.
[41] S. Manori, P. Singh, P. Yadav, A. Kumar, R. Chandra, K.K. Raina, R.K. Shukla, Magnetically tunable rheological properties of PVDF doped with superparamagnetic Fe_3O_4 nanoparticles synthesized by rapid microwave method, J. Phys. Chem. Solid. 174 (2023) 111137.
[42] M. Rakchana, S. Muthukumaran, Elevated visible light driven photo-catalytic properties of Ni-doped Bi_2WO_6 via hydrothermal technique, J. Phys. Chem. Solid. 208 (2026) 113127.
[43] A. Raza, I.A. Khan, A. Farid, Enriched pseudocapacitive performance of CVD deposited $MoSe_2/MoS_2$ heterostructured binder free nanospheres for asymmetric supercapacitor applications, J. Phys. Chem. Solid. 208 (2026) 113138.
[44] W. Shahzad, R. Hassan, A.K. Badawi, B. Ismail, Novel insights from XRD and photophysical properties of Cu_2ZnSnS_4: na thin films deposited by aqueous chemical route, J. Phys. Chem. Solid. 208 (2026) 113116.
[45] S. Tharuman, P. Vajeeston, S.-M. Chen, S. Baskaran, Self powered real time sustainable energy harvesting and sensing using NiCo-Prussian blue analogue–based triboelectric nanogenerator, Chem. Eng. J. 520 (2025) 165706.
[46] J. Tauc, R. Grigorovici, A. Vancu, Optical properties and electronic structure of amorphous germanium, Phys. Status. Solidi. 15 (1966) 627.
[47] S. Kar, S. Ghosh, T. Pal, MoS_2-CdS composite for photocatalytic reduction of hexavalent chromium and thin film optoelectronic device applications, Sci. Rep. 14 (2024) 18674.
[48] S. Ghosh, S. Kar, T. Pal, S. Ghosh, Sunlight - driven photocatalytic degradation of norfloxacin antibiotic in wastewater by ZnSe microsphere functionalized RGO composite, Sustain. Chem. Environ. 4 (2023) 100038.
[49] S. Tao, W. Zhong, F. Chen, P. Wang, H. Yu, Dispersible $CdS_{1-x}Se_x$ solid - solution nanocrystal photocatalysts: photoinduced self - transformation synthesis and enhanced hydrogen evolution activity, J. Colloid Interface Sci. 627 (2022) 320–331.
[50] D. Kiani, I.E. Wachs, Practical considerations for understanding surface reaction mechanisms involved in heterogeneous catalysis, ACS Catal. 14 (2024) 16770–16784.
[51] B. Liu, X. Zhao, C. Terashima, A. Fujishima, K. Nakata, Thermodynamic and kinetic analysis of heterogeneous photocatalysis for semiconductor systems, Phys. Chem. Chem. Phys. 16 (2014) 8751–8760.
[52] S. Ghosh, S. Kar, T. Pal, S. Ghosh, MoS_2-CdS composite photocatalyst for enhanced degradation of norfloxacin antibiotic with improved apparent quantum yield and energy consumption, J. Phys. Chem. Solid. 193 (2024) 112144.
[53] S. Cao, L. Piao, Considerations for a more accurate evaluation method for photocatalytic water splitting, Angew. Chem. Int. Ed. 59 (2020) 18312–18320.
[54] C.-W. Bai, F.-Q. Yang, P.-J. Duan, Z.-Q. Zhang, Y.-J. Sun, X.-J. Chen, F. Yu, H. Q. Chen, Dynamic in-situ reconstruction of active site circulators for photo-fenton-like reactions, Nat. Commun. 16 (2025) 3019.
[55] S. Khademakbari, A.E. Pirbazari, F.E.K. Saraei, A. Esmaeili, A.E. Pirbazari, A. A. Kohnehsari, A. Derakhshesh, Designing of plasmonic 2D/1D heterostructures for ultrasound assisted photocatalytic removal of tetracycline: experimental results and modelling, J. Alloys Compd. 975 (2024) 172994.
[56] S. Kar, T. Pal, S. Ghosh, Reduced graphene oxide - SnSe nanocomposite photocatalyst with high apparent quantum yield for the photodegradation of norfloxacin, ACS Appl. Nano Mater. 7 (2024) 6516–6524.
[57] S. Kar, T. Pal, S. Ghosh, Removal of norfloxacin from wastewater by adsorption onto SnS_2 followed by photocatalytic degradation, ChemistrySelect 8 (2023) e202300878.
[58] A. Trenczek-Zajac, M. Synowiec, K. Zakrzewska, K. Zazakowny, K. Kowalski, A. Dziedzic, M. Radecka, Scavenger-supported photocatalytic evidence of an extended type I electronic structure of the $TiO_2@Fe_2O_3$ interface, ACS Appl. Mater. Interfaces 14 (2022) 38255–38269.
[59] A. Cabona, S. Toso, A. Griesi, M. Rizzo, M. Ferri, P. Rusch, G. Divitini, J. Pérez-Prieto, R.E. Galian, I. Kriegel, L. Manna, Synthesis, growth mechanism, and photocatalytic properties of metallic-Bi/$Bi_{13}S_{18}Br_2$ nano-bell heterostructures, ACS Mater. Lett. 7 (2025) 1707–1716.
[60] P. Zeng, X. Ji, Z. Su, S. Zhang, WS_2/g-C_3N_4 composite as an efficient heterojunction photocatalyst for biocatalyzed artificial photosynthesis, RSC Adv. 8 (2018) 20557–20567.